Suppressing the spectral shift of a polarization-independent nanostructure with multiple resonances

Dipa Ghindani, Tuomas Pihlava, and Humeyra Caglayan*

Faculty of Engineering and Natural Sciences, Tampere University, Tampere 33720, Finland
*Corresponding author: humeyra.caglayan@tuni.fi

Resonances are the cornerstone of photonic applications in many areas of physics and engineering. The spectral position of a photonic resonance is dominated by the structure design. Here, we devise a polarization-independent plasmonic structure comprising nanoantennas with two resonances on an epsilon-near-zero (ENZ) substrate in order to loosen this correlation to obtain less sensitivity to geometrical perturbations of the structure. Compared with the bare glass substrate, the designed plasmonic nanoantennas on an ENZ substrate exhibit a nearly three-fold reduction only in the resonance wavelength shift near the ENZ wavelength as a function of antenna length.

Introduction. Resonant optical devices play a significant role in the rapid development of nanotechnology and photonics-based technologies. Numerous applications such as filters [1,2], switches [3], modulators [4], and sensors [5] are realized by employing resonant devices. In addition to these applications, resonances are vital for studying several fundamental phenomena such as ultra-strong coupling [6] and nonlinear effects [7,8]. In principle, the resonance wavelength of a plasmonic antenna is significantly influenced by its shape, dimensions, and local environment, particularly its substrate [9–11], which can be a great advantage for sensing applications. However, the resonance modes are prone to geometrical inhomogeneity, this may arise as an issue for the fabrication or packaging of the integrated devices. Therefore, it is imperative to develop a novel way to endow the robustness of the plasmonic resonance from the geometrical perturbation for certain applications.

In recent years, the investigation of epsilon-near-zero (ENZ) materials in plasmonic systems has provided a great platform from the beam shaping to long-range qubit entanglement [12–19]. One particular concept is using the ENZ materials as a substrate as a means of reducing the index of the substrate, and because of the high dispersion of ENZ, the sensitivity of the plasmonic resonance on geometrical parameters can be reduced

significantly [20–25]. Slowing down the change in the plasmonic resonances near the ENZ wavelength, an effect referred to as resonance pinning, has been shown with an ENZ substrate such as Al-doped ZnO (AZO), indium tin oxide (ITO) and SiC [20,22,23], and using a hyperbolic ENZ metamaterial [21].

In this work, we investigate elongated nanoantenna arrays that support two resonances: one in the ENZ region while the other one is out of the ENZ region. The spectral shift of the plasmonic antenna exhibits the pinning effect only for the resonances close to the ENZ region. Therefore, this is especially a strong method when one wants to fix one of the resonances but not all of them when interacting with unpolarized light. We experimentally explored and characterized plasmonic antennas that are designed to exhibit polarization-independent dual resonances, one of them lies within the ENZ wavelength region and the other is spectrally far from the ENZ region. We further compared the resonance characterization of a plasmonic nanoantenna on a glass substrate (non-zero effective index). Our results show the utilization of ENZ materials for increasing the versatility and functionality of plasmonic structures. Additionally, our approach can be exploited to manipulate the resonance for advanced nanostructures and plasmonic applications, especially selectively controlling one of the resonances of the nanoantenna array designs for an unpolarized illumination.

Results and discussion. For probing the influence of ENZ properties upon local plasmon resonance, we utilized a commercially available 100 nm-thick ITO on glass as an ENZ substrate. An ITO is the widely used transparent conducting oxide (TCO) that exhibits a vanishing real part of the permittivity in the near-infrared spectral region with remarkably low optical losses. To characterize the dispersion of an ITO, we performed the spectroscopic ellipsometry measurement on 100 nm ITO thick film and extracted the complex permittivity. In Fig. 1(a), the real and imaginary parts of the 100 nm ITO thick film's permittivity are shown as the blue and red solid lines, respectively. The real part of the permittivity vanishes at 1320 nm and is marked as ENZ wavelength $\lambda_{ENZ} = 1320$ nm. The near-zero permittivity (eps ≈ 0) region that spans from 1120 to 1520 nm is highlighted by a gray shaded region in Fig. 1(a).

In order to achieve two resonances, it is possible to bring two structures with different dimensions into a single unit cell, or one can take advantage of an elongated structure such as an
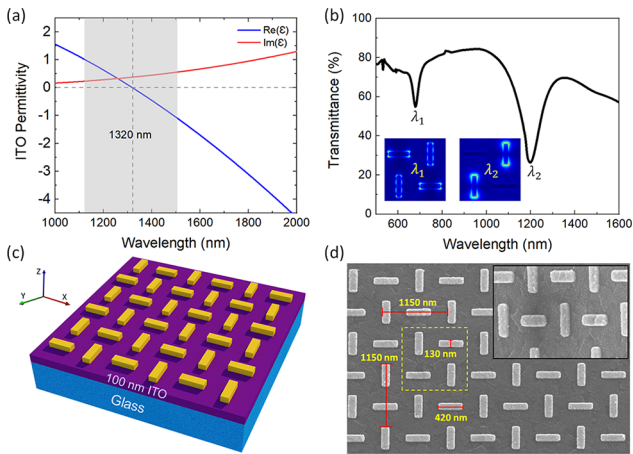
Fig. 1. (a) Experimentally recorded complex permittivity of 100 nm-thick ITO film. The blue and red solid lines depict the real and imaginary parts of the ITO's permittivity, respectively. (b) Simulated transmittance spectra of the plasmonic nanoantennas on the ITO substrate; the insets depict the electric field profile at the corresponding wavelength. (c) Schematic of polarization-independent Au nanoantenna array of thickness 40 nm on a 100 nm-thick ITO layer on a glass substrate. (d) Scanning electron microscope (SEM) image shows the top view of the Au nanoantenna array (scaling factor = 1, i.e., l_s = 130 nm and l_l = 420 nm); the dashed yellow box indicates the supercell with supercell periodicity 1150 nm in the *x* and *y* directions. The inset shows the SEM image taken at 30° tilt.

ellipse or rectangle. Here, we utilized a rectangular nanoantenna that can provide two plasmon resonances: TSPR (transversal surface plasmon resonance) and LSPR (longitudinal surface plasmon resonance). Furthermore, through the combination of the nanoantennas in two different orientations, we finalized the supercell design. We performed finite-difference time-domain (FDTD) numerical simulations to optimize nanoantenna dimensions and supercell periodicity. The experimentally recorded permittivity of the ITO is fed into the simulations, and was modeled by using Johnson and Christy material data from the in-build material library of Ansys Lumerical. The boundary conditions are set to periodic in the *x* and *y* directions and perfectly matched layers (PMLs) in the direction perpendicular to the source propagation (*z*). For any incident polarization, there exist two dipole resonances in the supercell, one corresponding to the long axis and another to the short axis of the elongated nanorods. This yields two spectrally distinct resonance dips in transmission spectra for any incident polarization (either *x* or *y*) as the design is rotationally symmetric, as shown in Fig. 1(b). We optimized the dimensions of the nanorods such that one resonance falls within the ENZ region of the ITO and the other resonance lies spectrally far from the ENZ region, shown in Fig. 1(b).

The transmission spectra corresponding to our devised polarization-independent plasmonic nanostructure shows the dips at shorter (λ_1 = 650 nm) and longer (λ_2 = 1200 nm) wavelengths in transmission spectra correspond to the dipole resonances along the short and long axes, respectively. The simulated electric field profiles corresponding to λ_1 and λ_2 are shown in inset of Fig. 1(b). From the electric field profile, it is evident that the dipole resonances for λ_1 and λ_2 are localized along the short and long axes, respectively.

Figure 1(c) shows the schematic of the ITO integrated polarization-independent plasmonic nanoantenna array. To emulate the polarization-independent response, the nanorods are alternatively arranged in two different orientations. To create these nanostructures with high precision, on glass and ITO substrates, we utilized electron beam lithography (EBL). In the glass substrate case, after spin coating PMMA 950K positive resist, the conducting polymer was spin-coated to avoid the charging effect. After exposure, both glass and ITO samples were developed in MIBK : IPA (1 : 3) solution. A 1 nm/40 nm layer of Ti/Au was deposited on developed samples using an electron beam metal evaporator followed by lift-off in S1165 remover. Figure 1(d) shows the SEM image of the top view of the fabricated plasmonic nanoantennas, where the supercell is marked by a yellow dashed square. The periodicity of the supercell along the *x* and *y* directions is *P* = 1150 nm, while the length of nanorod along short (l_s) and long (l_l) axes are l_s = 130 nm and l_l = 420 nm and the thickness of the nanorod is 40 nm. We employed gold (Au) as the plasmonic material owing to low loss and ease of deposition.

By varying the length of the nanorods in the supercell, i.e., scaling with a common factor that varied between 0.8 and 1.2 and keeping the periodicity constant, the plasmonic resonance response can be tuned systematically. The optimized spatial dimensions of the plasmonic nanorod that corresponds to scaling factor "1" are l_s = 130 nm and l_l = 420 nm. Further, we fabricated a set of samples on both the ITO substrate and bare glass substrate with varying scaling factors from 0.8 to 1.2, the SEM images are shown in Fig. 2(a). For varying the scaling factors, the
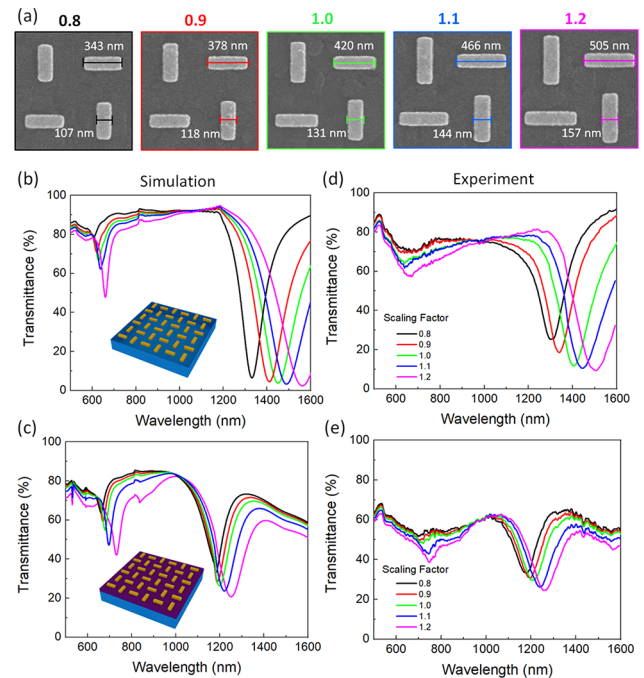

Fig. 2. (a) SEM images of the fabricated set of samples with varying scaling factors from 0.8 to 1.2 and a constant periodicity of 1150 nm in both *x* and *y*. (b),(c) Simulated transmittance spectra of the supercell array of nanorods on a glass and ITO substrate for various scaling factors (0.8 to 1.2); the inset shows a schematic of the Au antenna array on glass and ITO, respectively. (d),(e) Experimentally recorded transmission spectra of the supercell array of nanorods on a glass and ITO substrate for various scaling factors of 0.8 to 1.2.

lengths of short and long axes change simultaneously; however, the periodicity of the supercell is fixed at $P = 1150$ nm. Figures 2(b) and 2(c) show the simulated transmission spectra for the plasmonic nanoantenna array upon incidence of unpolarized light for bare glass and ITO substrate, respectively, at different scaling factors. The simulated results clearly illustrate that the resonance wavelength that lies within the ENZ region of the ITO substrate (λ_2) exhibits much less sensitivity to dimension change as compared with the bare glass substrate.

To further verify this, we experimentally recorded the transmission spectra for all the fabricated plasmonic nanorod array using a multifunctional WITec alpha300C confocal Raman microscope. For both nanoantennas fabricated on ITO film and on a glass substrate, the transmission was normalized to the transmission spectrum of glass. The results corresponding to nanostructures on the bare glass and ITO substrate are shown in Figs. 2(d) and 2(e), respectively. The experimental results show good agreement with the simulation results for both cases. The small difference in simulated and experimental transmission spectra at the shorter wavelength around 650 nm, e.g., resonance broadening, can be attributed to the fabrication imperfections such as slight inhomogeneity, rounding the edge of the nanoantenna, and experimental noise in the visible range due to the detector. Importantly, the experimental results confirm the effect of the ENZ on the resonance. The change in plasmonic resonance that lies within the ENZ region of ITO, i.e., λ_2 exhibits nearly 80 nm spectral shift when changing the scaling factor from 0.8 to 1.2, while the plasmonic nanorod on bare glass substrate shows 225 nm shift in resonance wavelength [see Figs. 2(d) and 2(e)]. It is important to note that the shift of resonance dip at a lower wavelength (λ_1) is similar for both ITO and bare glass substrate.

To illustrate the shift in resonance wavelength more clearly, we plotted the change in resonance wavelength ($\Delta\lambda$) as a function of the scaling factor. Figure 3 compares the shift in resonance wavelengths numerically as well as experimentally. Figures 3(a) and 3(b) depict the $\Delta\lambda$ for lower resonance (λ_1), where the black and red lines represent the resonance wavelength of the plasmonic nanorod on bare glass and ITO substrate, respectively. As is clear from Figs. 3(a) and 3(b), the shift in lower wavelength resonance is nearly identical for both cases. However, the shift in longer wavelength resonance, which lies within the ENZ region of ITO, exhibits less susceptibility toward geometrical changes when it is fabricated on an ENZ substrate. Figures 3(c) and 3(d) reveal that the spectral shift in longer wavelength resonance on the ITO substrate is three times less compared with the resonance shift on a bare glass substrate. This slowdown in the change in resonance wavelength is attributed to the resonance pinning around the ENZ wavelength.

To understand the underlying physics behind the resonance pinning effect, we express the rate of change of resonance wavelength as a function of antenna length [23] as

$$\frac{\delta\lambda}{\delta l} = A\frac{n^2}{n - \lambda_0\frac{\delta n}{\delta \lambda}}, \tag{1}$$

where n is the effective index, A is constant, and λ_0 is the free space wavelength. For the non-dispersive medium, i.e., $\delta n / \delta\lambda = 0$, the resonance wavelength becomes proportional to the length of the nanoantenna and the index ($\lambda \propto Anl$).

We numerically calculated the effective mode index of the nanorod on the ITO substrate and glass substrate using a finite-difference eigenmode (FDE) mode solver in Ansys. The
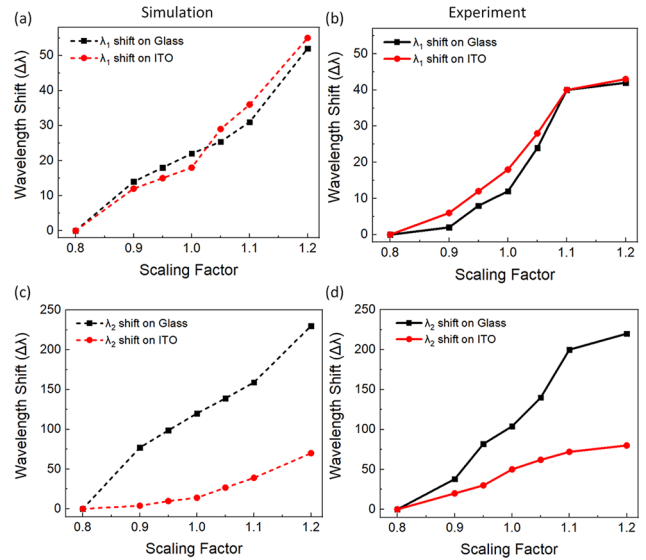

Fig. 3. (a),(b) Simulated and experimental wavelength shift result ($\Delta\lambda$) as a function of scaling factor, respectively, at resonance 1 (λ_1) at a shorter wavelength. (c),(d) Simulated and experimentally recorded wavelength shifts, respectively, corresponding to resonance 2 (λ_2) at a longer wavelength.
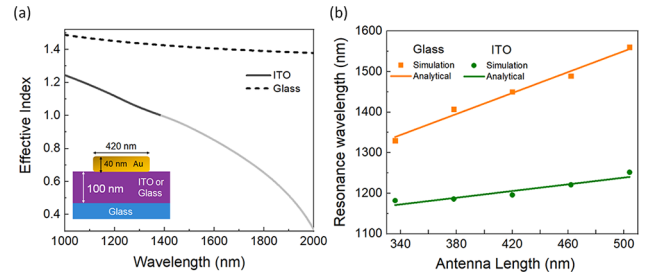

Fig. 4. (a) Numerically calculated effective mode index for a gold nanorod on the ITO (black solid line and values below unity are colored in gray) and a glass substrate (black dashed line). The inset shows the configuration of the finite-element solver. (b) Resonant wavelength (λ) as a function of antenna length (l_l) for the glass (orange) and ITO (green) substrates. The solid lines are calculated analytically, and square and circular markers are the results of FDTD numerical calculations.

calculated results are shown in Fig. 4(a), which reveal that the effective index of the nanorod on the ENZ substrate has strong negative dispersion and is less than unity for the wavelength past the ENZ wavelength of ≈ 1320 nm. We noticed that the effective index value is below unity at higher wavelengths, which is not physical and arises due to the approximations of the boundary conditions in the numerical calculation, therefore, we colored that part gray. On the contrary, the effective index of the nanorod on a glass substrate is nearly constant (i.e., weakly dispersive) with a value close to ≈ 1.46. The pinning effect is due to a reduction in the effective mode index and highly negative dispersive nature of the ENZ substrate, which limits the spectral shift of the nanorod antenna beyond the ENZ region.

Furthermore, Fig. 4(b) shows a comparative plot of the resonance wavelength for bare glass and ITO substrate. The resonance wavelength (λ) is plotted against antenna length (l_l) analytically according to the relation in Ref. [23], which is based

on the Fabry–Perot model. The square and circular markers depict the resonance wavelength extracted using FDTD numerical calculations. The simulation results show good agreement with these analytical results.

Conclusion and outlook. We devised a plasmonic nanoantenna exhibiting a polarization-independent spectral response. By incorporating the plasmonic structure with an ITO substrate, we showed the spectral pinning of plasmonic resonance within the ENZ region. To showcase this experimentally, we judiciously designed a plasmonic nanoantenna array that yields dual resonances: one lies within the ENZ region, and the other exists spectrally far from the ENZ region. Our results reveal that the shift in resonance wavelength for the plasmonic nanorod array fabricated on ITO substrate exhibits less susceptibility toward geometrical changes. We benchmarked the performance of the plasmonic nanoantennas devised on ITO substrate with the nanoantennas on a bare glass substrate. We showed the spectral shift of the polarization-independent nanoantennas suppressing by approximately three times in the case of the ITO substrate due to the near-zero index of the substrate. We verified numerically, analytically, and experimentally that the shift in resonance wavelength becomes nearly independent of the antenna length near the ENZ wavelength. This control over plasmon resonance and the reduced dependence on antenna dimensions relax the requirement of precise subwavelength features. Furthermore, less sensitivity of the nanoantenna's resonance toward its length results in a narrow spectral bandwidth, which is important for sensing, color filtering, and switching applications. However, some applications, such as data communication which requires large bandwidth, may not benefit.

Additionally, we demonstrate the universality of the pinning effect by showing the slowing down of resonance near the ENZ point in a multi-resonance plasmonic system. Also, selectively controlling one of the resonances of the nanoantenna designs for unpolarized illumination is of great importance for advanced plasmonic applications. Our approach can compensate for fabrication errors, reduce the need for advanced fabrication, and increase flexibility in plasmonic nanoantenna designing. The demonstrated results pave the path for utilizing ENZ materials to increase the versatility and functionality of plasmonic structures and provide foundational insight into this exotic material phenomenon. Moreover, we foresee the plasmon resonance wavelength being adjusted by dynamically tuning the permittivity of the substrate around the ENZ point via optical or electrical control in both reflection and transmission modes, allowing more functional implementations of this platform.

REFERENCES

1. T. Xu, Y.-K. Wu, X. Luo, and L. J. Guo, Nat. Commun. **1**, 59 (2010).
2. D. Ghindani, I. Issah, S. Chervinskii, M. Lahikainen, K. Kuntze, A. Priimagi, and H. Caglayan, ACS Photonics **9**, 2287 (2022).
3. S. Sederberg, D. Driedger, M. Nielsen, and A. Elezzabi, Opt. Express **19**, 23494 (2011).
4. Q. Xu, B. Schmidt, S. Pradhan, and M. Lipson, Nature **435**, 325 (2005).
5. X. Ma, S. Fan, H. Wei, Z. Zuo, S. Krishnaswamy, and J. Fang, Opt. Express **27**, 33051 (2019).
6. P. Forn-Díaz, L. Lamata, E. Rico, J. Kono, and E. Solano, Rev. Mod. Phys. **91**, 025005 (2019).
7. G. Li, S. Zhang, and T. Zentgraf, Nat. Rev. Mater. **2**, 17010 (2017).
8. Y. Yang, W. Wang, A. Boulesbaa, I. I. Kravchenko, D. P. Briggs, A. Puretzky, D. Geohegan, and J. Valentine, Nano Lett. **15**, 7388 (2015).
9. B. Gerislioglu, L. Dong, A. Ahmadivand, H. Hu, P. Nordlander, and N. J. Halas, Nano Lett. **20**, 2087 (2020).
10. B. C. Yildiz, M. Habib, A. R. Rashed, and H. Caglayan, J. Appl. Phys. **126**, 113104 (2019).
11. F. J. González and J. Alda, Opt. Commun. **284**, 1429 (2011).
12. I. Issah, M. Habib, and H. Caglayan, Nanophotonics **10**, 4579 (2021).
13. L. Caspani, R. P. M. Kaipurath, M. Clerici, M. Ferrera, T. Roger, J. Kim, N. Kinsey, M. Pietrzyk, A. Di Falco, V. M. Shalaev, A. Boltasseva, and D. Faccio, Phys. Rev. Lett. **116**, 233901 (2016).
14. D. Ghindani, A. R. Rashed, M. Habib, and H. Caglayan, Adv. Opt. Mater. **9**, 2100800 (2021).
15. V. Bruno, C. DeVault, S. Vezzoli, Z. Kudyshev, T. Huq, S. Mignuzzi, A. Jacassi, S. Saha, Y. D. Shah, S. A. Maier, D. R. S. Cumming, A. Boltasseva, M. Ferrera, M. Clerici, D. Faccio, R. Sapienza, and V. M. Shalaev, Phys. Rev. Lett. **124**, 043902 (2020).
16. M. Z. Alam, I. D. Leon, and R. W. Boyd, Science **352**, 795 (2016).
17. I. Liberal and N. Engheta, Nat. Photonics **11**, 149 (2017).
18. X. Niu, X. Hu, S. Chu, and Q. Gong, Adv. Opt. Mater. **6**, 1701292 (2018).
19. S. Campione, J. R. Wendt, G. A. Keeler, and T. S. Luk, ACS Photonics **3**, 293 (2016).
20. J. Kim, A. Dutta, G. V. Naik, A. J. Giles, F. J. Bezares, C. T. Ellis, J. G. Tischler, A. M. Mahmoud, H. Caglayan, O. J. Glembocki, A. V. Kildishev, J. D. Caldwell, A. Boltasseva, and N. Engheta, Optica **3**, 339 (2016).
21. M. Habib, D. Briukhanova, N. Das, B. C. Yildiz, and H. Caglayan, Nanophotonics **9**, 3637 (2020).
22. X. Duan, F. Zhang, Z. Qian, H. Hao, L. Shan, Q. Gong, and Y. Gu, Opt. Express **27**, 7426 (2019).
23. C. T. DeVault, V. A. Zenin, A. Pors, K. Chaudhuri, J. Kim, A. Boltasseva, V. M. Shalaev, and S. I. Bozhevolnyi, Optica **5**, 1557 (2018).
24. O. Dominguez, L. Nordin, J. Lu, K. Feng, D. Wasserman, and A. J. Hoffman, Adv. Opt. Mater. **7**, 1800826 (2019).
25. S. A. Schulz, A. A. Tahir, M. Z. Alam, J. Upham, I. De Leon, and R. W. Boyd, Phys. Rev. A **93**, 063846 (2016).